CALCULATIONS OF HIGH SPEED PROPELLER PERFORMANCES USING FINITE DIFFERENCE METHODS

ICAS-86-3.10.3

M. Kobayakawa, H. Onuma and Y. Shiota
Kyoto University
Kyoto, Japan

Abstract

In order to examine flowfield around ATP by numerical caculations, the finite difference methods are applied. In the first part, the partial differential equation for the disturbance velocity potential is solved by line relaxation technique. In order for the calculations, boundary fitted meshes are generated. The transformations between physical space and computational one are performed by chain rule. SR-3 is used for numerical calculations. In the second part, the Euler equations are solved by non-iterative implicit ADI schemes in AF algorithm. Boundary fitted meshes are also used for this case. The results show qualitative agreement with the results by Bober et al. Finally, the aerodynamic performances, such as power coefficients and efficiencies, are obtained. Potential calculations show that these quantities take relatively larger than the experimental values obtained by NASA, however, Euler solutions show that the values come closer to the experimental values.

1. Introduction

Studies and developments of Advanced Turbo-Prop (ATP) are progressing promptly, and are spreading over the world. It is said that FTB program or flight test for practical use will be soon realised. NASA already finished their wind-tunnel tests, and these are continued in other countries now. We can see some papers of theoretical research works and the number of them will increase hereafter. Among many advantages of theoretical investigations about the aerodynamic performance of ATP, the most prominent one is to obtain the flow detail around very complex configuration of ATP with accuracy. This is difficult for the wind-tunnel tests.

Sullivan[1] calculated ATP performances by the lifting line theory, and Hanson[2] by the lifting surface theory. The author[3] calculated the aerodynamic performances by the VLM (vortex lattice method) up to flight Mach number of 0.6. Since CPU time of these calculations is not so long, it is easy to get characteristic curves of ATP. However, it is impossible to calculate its performance in transonic range, i.e. Mach 0.8, where shock wave may occur. For this speed range, the finite difference methods for transonic flow should be applied to ATP. Jou[4] calculated the flowfield around SR-1 applying a finite volume method to a potential equation. Chaussee and Kutler[5] presented a method of calculation for SR-3 by solving 3D-Euler equations and Bober et al.[6] got the results. Bousquet[7] obtained the flow field around the ONERA's ATP by solving 3D-Euler equations.

In this paper, the flowfield around an ATP, SR-3, is calculated by solving a potential equation and Euler equations, and its aerodynamic performances are obtained. Since CPU time is short, the potential analysis is very convenient for this purpose. Using vector processor, CPU time of VLM for one case of a pictch angle of three-quarter of the tip radius and an advance ratio is about 2 minutes, and that of this method is about 15 minutes. On the other hand, CPU-time for Euler equations is over 30 minutes. The numerical calculations are performed for SR-3 in flight Mach number 0.8 for three kinds of pitch angle of three-quarter of the tip radius, 57.3, 59.3 and 61.3 deg., and advance ratios are varied from 3 to 4. The results are compared with the values of the wind tunnel test performed at NASA[8].

2. Method by Potential Equation

2.1 Basic Equations

The flowfield of an ATP moving in the air with a constant flight speed and a constant rotating speed is unsteady from the view point of a static frame. However, it is steady based on the rotating frame fixed on a propeller blade, and if the effect of viscosity is confined within the boundary layer on the solid surface and the thin wake shed from the blade trailing edge, and, moreover, if shock wave standing on the blade surface is weak, the nonviscous and isentropic assumptions can be made. On the rotating frame fixed on a blade, free stream to the ATP becomes rotating flow. Therefore, there exists no velocity potential. However, a disturbance velocity potential can be assumed for the relative flow around the nacelle and blades.

Let the system of rotating axes be fixed on a blade shown in Fig.1, i.e. x-axis is adverse direction of ATP motion, y-axis spanwise direction and z-axis is taken to be right handed system with x and y axes. The equation for the disturbance velocity potential is written as follows:

$$(a^2 - u^2)\phi_{xx} + (a^2 - v^2)\phi_{yy} + (a^2 - w^2)\phi_{zz} - 2uv\phi_{xy} - 2vw\phi_{yz} - 2wu\phi_{zx} = 0 \qquad (1)$$

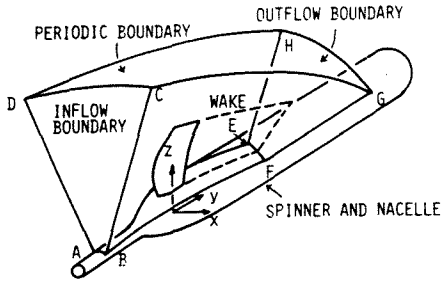

Fig.1 Physical space and coordinate axes

And the energy equation is written as follows:

$$a^2 = \frac{1}{M_\infty^2} - \frac{\gamma - 1}{2}\left[|v|^2 - |V|^2\right], \qquad (2)$$

where the free stream velocity V and local velocity v are given by

$$V = [\ 1,\ -\frac{\pi}{J}z\ ,\ \frac{\pi}{J}y\ ] \tag{3}$$

$$v = [\ u,\ v,\ w\ ]$$

$$= [\ 1 + \phi_x\ ,\ -\frac{\pi}{J}z + \phi_y\ ,\ \frac{\pi}{J}y + \phi_z] \tag{4}$$

a is local speed of sound, M_∞ flight Mach number and J advance ratio.

$$M_\infty = \frac{V_\infty}{a_\infty} \tag{5}$$

$$J = \frac{\pi V_\infty}{\Omega R}\ ,\quad \Omega : \text{angular velocity} \tag{6}$$

In these equations, lengths and velocities are non-dimensionalized by the propeller radius R and flight speed V_∞ respectively.

The main part of this work is to solve the equation of disturbance potential ϕ, Eq.(1). As a result, the pressure coefficient based on the density and pressure at infinity can be calculated by the following equation.

$$C_p = \frac{2}{\gamma M_\infty^2}[\{1 - \frac{\gamma - 1}{2}M_\infty^2(|v|^2 - |V|^2)\}^{\frac{\gamma}{\gamma-1}} - 1] \tag{7}$$

By this equation, the ATP aerodynamic performances, power coefficients and efficiencies, can be calculated.

2.2 Mesh Generations

In order to solve the partial differential equation for the disturbance velocity potential, Eq(1). by finite difference method, it is necessary to generate a computational mesh in the space around the ATP. In this paper, the boundary fitted meshes are generated. Generally, ATP has many blades with same configurations which are distributed by equal angles around rotating axis. When the flight direction is parallel with this axis and the spinner and nacelle are axisymmetric, the flowfield around all blades are same, i.e. a flowfield is periodic circumferentially. In solving this flowfield, it is usual that the space between two blades neighbouring with each other is treated for calculation. It is the calculation technique for cacades such as turbine blades. However, for this potential calculations, the space including a blade is employed. In other words, we intend to solve the flowfield around a blade and nacelle. The physical space of calculation is shown in Fig.1. For the Euler calculations, the space between the neighboring blades is chosen. This case will be described in the next chapter.

Actual configuration of an ATP blade is determined by chord length, sectional form and thickness of airfoil in the surface normal to y axis, pitch angle and sweep angle at a quarter chord line. In order to generate meshes around ATP with these complex configurations, the following processes are performed. First, the space of Fig.1 is divided into many axisymmetric surfaces. Second, the two-dimensional H-type periodic meshes are generated for an airfoil which is cross sectional form of the axisymmetric surface and the balde. Finally, three-dimensional meshes are generated by connecting the above two-dimensional grids radially.

To avoid discontinuity of meshes in the outer region of the blade, a hypothetical blade is considered. This hypothetical blade has zero thickness, and chord length becomes larger in the outer portion, and pitch angle is taken for angle of attack to be zero relative the flow. The enlargement of the chord length is to moderate mesh density. In the calculations, the grid points of this hypothetical blade are treated as flow point.

The configurations of spinner and nacelle are determined by their radius distribution $r_H(x)$ along the axis of rotation. In order to avoid the singular point at the top of the spinner, the circular cylinder with small radius is extended to the forward infinity. The following transformation is introduced[9].

$$r^* = r - [\ r_H(x) - R_H]\ \frac{r_T - r}{r_T - r_H(x)}\ ,$$

$$(\ r_H(x) \le r \le r_T\ ), \tag{8}$$

where r_H is the radius of the blade and r_H is nacelle radius after transformation which is constant. By Eq.(8), the axisymmetric space between nacelle and r_H is transformed into the regions between cylinders from r_H to r_H. The outer part from the blade tip is transformed by identical one.

$$r^* = r\ ,\quad (\ r > r_T\ ) \tag{9}$$

The next step is that the region of $R_H \le r^* \le r_H$ is divided into equidistant parts, and the region of $r^* \ge r_H$ is divided into exponentially extending parts. Consequently, the several cylindrical surfaces are made. The intersections of the blade surfaces and these cylindrical surfaces can be obtained by interpolations of some sample points of the blade surface. There appeared airfoils on the developed cylindrical surfaces. Then, H-type periodical meshes are generated. For this mesh generation, a conformal mapping is utilized for the leading edge of the airfoil. Mapping function is given by

$$\bar{Z} = i\zeta^{1/2} + k\zeta, \tag{10}$$

where

$$\bar{Z} = \bar{X} + i\bar{Y}$$

$$\zeta = \xi + i\eta \tag{11}$$

In Eqs.(10) and (11), the origin of coordinate axes is at leading edge. This mapping function is effective to airfoil with large leading edge curvature such as this case (NACA 16 series airfoil section). Generated meshes are shown in Figs.2(a), (b) and (c), which correspond to X-, Y- and Z-constant planes in the computational domain (Fig.3) respectively.

2.3 Computational Domain and Boundary Conditions

Eq.(1), the equation for disturbance velocity potential, is solved in the computational domain shown in Fig.3. All grid durations are unity, i.e. $\Delta X = \Delta Y = \Delta Z = 1$. Once the meshes are built up, the physical coordinates x, y and z are easily related to the computational coordinates X, Y and Z by chain rule. The derivatives are described by Chen[4] in detail. Therefore, Eq.(1) is transformed in the computational domain as follows:

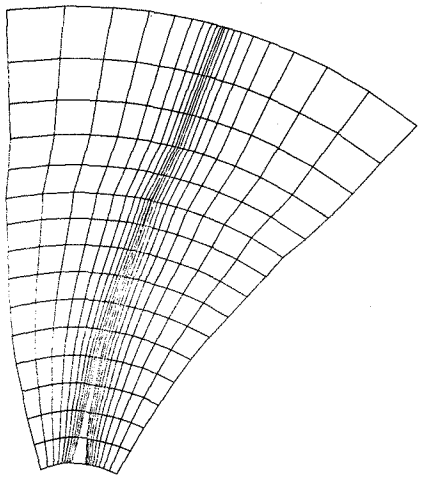

(a) X -constant plane

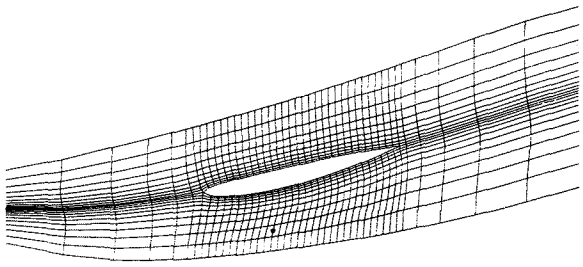

(b) Y -constant plane

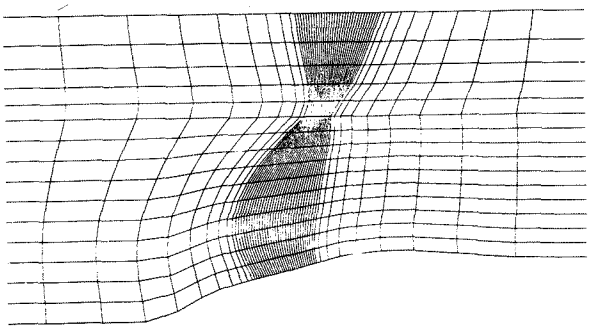

(c) Z -constant plane

Fig.2 Meshes around the SR-3 propeller

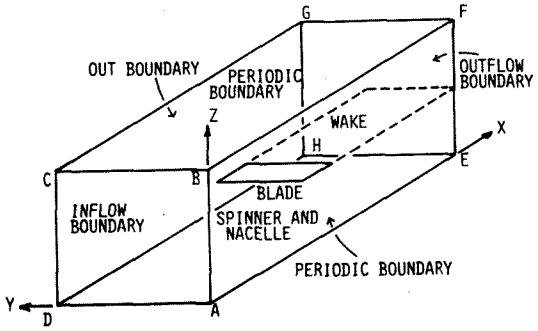

Fig.3 Computational domain

$$C_1\phi_{XX} + C_2\phi_{YY} + C_3\phi_{ZZ} + C_4\phi_{XY} + C_5\phi_{YZ} + C_6\phi_{ZX} + C_7\phi_X + C_8\phi_Y + C_9\phi_Z = 0, \quad (12)$$

where $C_1, C_2, \ldots, C_9$ are expressed by the contravariant vector $(U\ V\ W)^T$ of the velocity $(u\ v\ w)^T$ and the derivatives x_X, x_Y etc.

Let us consider the boundary conditions. On the inflow boundary ABCD and out boundary DCGH (Fig.1 or Fig.3), disturbance velocity potential should be zero.

$$\phi = 0 , \quad \text{(inflow and out boundaries)} \quad (13)$$

On the outflow boundary EFGH, when the flow is subsonic, the following equation is applied.

$$C_2\phi_{YY} + C_3\phi_{ZZ} + C_5\phi_{YZ} + C_8\phi_Y + C_9\phi_Z = 0 ,$$

$$\text{(outflow, subsonic)} \quad (14)$$

This equation is obtained from Eq.(12) by neglecting all X derivatives. This means no streamwise variation in the outflow boundary. However, Eq.(14) is not applied when the flow is supersonic. On the solid surface, spinner and nacelle and blade surfaces, the impermeability conditions are applied.

$$V = 0 , \quad \text{(spinner and nacelle surfaces)} \quad (15)$$

$$W = 0 , \quad \text{(blade surfaces)} \quad (16)$$

$$V = W = 0 , \quad (17)$$

(intersections of the nacelle and the blade)

At the trailing edge, Kutta condition is applied in general cases. However, in this paper, Eq.(16) is applied at this point.

The condition at the blade tip should be given. Chen[10] expresses this by

$$\phi_{ZZ} = 0 , \quad \text{(blade tip)}, \quad (18)$$

just outboard of the tip. In this paper, at first, the calculations were performed using this condition. The grid line just outboard of the blade tip was laid at 1.001R (R is blade radius). The results showed that the pressure distribution along this grid line took strange form. Consequently, the grid line was removed to just inboard of the tip, 0.999R, and the condition Eq.(15) is applied for the blade tip condition.

The potential jump across the wake is assumed to be constant and its value is difference of potentials between the upper and lower sides at the trailing edge. Thickness of the wake is assumed to be zero. Finally, on the periodic boundaries, the potential values are equal with each other, i.e.

$$\phi_{AEHD} = \phi_{BFGC} , \quad \text{(periodic boundaries)} \quad (19)$$

2.4 Method of Numerical Calculations

In solving Eq.(1), if the flow direction is approximately x axis, it is sufficient to take upwind difference along x direction in supersonic region. However, the flow around the ATP is highly inclined and the equation should be

rewritten by an orthogonal coordinate system with one coordinate s aligned with the flow direction as follows:

$$(a^2 - q^2)\phi_{ss} + a^2(\nabla^2\phi - \phi_{ss}) = 0 \tag{20}$$

where

$$q^2 = u^2 + v^2 + w^2 \tag{21}$$

Representing ϕ_{ss} by x, y and z, it is expressed by

$$\phi_{ss} = \frac{1}{q^2}(u^2\phi_{xx} + v^2\phi_{yy} + w^2\phi_{zz} + 2uv\phi_{xy} + 2vw\phi_{yz} + 2wu\phi_{zx}) \tag{22}$$

In Eq.(20), ϕ_{ss} in the first term should be calculated by upwind difference in supersonic region. Here, the artificial viscosity is added as the directional bias of supersonic flow as follows:

$$\begin{aligned} &C_1(\phi_{XX})_{CD} + C_2(\phi_{YY})_{CD} + C_3(\phi_{ZZ})_{CD} \\ &+ C_4(\phi_{XY})_{CD} + C_5(\phi_{YZ})_{CD} + C_6(\phi_{ZX})_{CD} \\ &+ C_7(\phi_X)_{CD} + C_8(\phi_Y)_{CD} + C_9(\phi_Z)_{CD} \\ &- \mu\{p_1[(\phi_{XX})_{UW} - (\phi_{XX})_{CD}] + p_2[(\phi_{YY})_{UW} - (\phi_{YY})_{CD}] \\ &+ p_3[(\phi_{ZZ})_{UW} - (\phi_{ZZ})_{CD}] + p_4[(\phi_{XY})_{UW} - (\phi_{XY})_{CD}] \\ &+ p_5[(\phi_{YZ})_{UW} - (\phi_{YZ})_{CD}] + p_6[(\phi_{ZX})_{UW} - (\phi_{ZX})_{CD}]\} \\ &= 0, \end{aligned} \tag{23}$$

where

$$\mu = \max\left(0,\ 1 - \frac{a^2}{q^2}\right), \tag{24}$$

and $p_1, p_2, \ldots, p_6$ are the coefficients expressed by the components of contravariant vector $(U\ V\ W)^T$. The subscript UW indicates upwind difference, CD central difference. The above artificial viscosity has nonconservation form.

All of the finite differences are second order and, especially, for UW,

$$(\phi_{XX})_{UW} = \phi_{i-2s_1,j,k} - 2\phi_{i-s_2,j,k} + \phi_{i,j,k},$$

$$s_1 = \ ; U > 0 \qquad s_1 = \ ; U < 0 \tag{25}$$

In order to solve Eq.(23), the line relaxation method is applied. It is vertical line relaxation in which ϕ at (i,j) point are unknowns. Let this value be ϕ^{+}_{ijk}, the (n+1)-th potential can be obtained by

$$\phi^{n+1}_{i,j,k} = \omega\phi^{+}_{i,j,k} + (1 - \omega)\phi^{n}_{i,j,k} \tag{26}$$

The iteration process is continued until the following relation is satisfied.

$$\max_{i,j,k}\left[\ |\phi^{n+1}_{i,j,k} - \phi^{n}_{i,j,k}|\ \right] < \varepsilon \tag{27}$$

where ε is a small quantity of convergence criterion. $C_1, C_2, \ldots, C_9$ and x_{XX}, x_{YY} included in $p_1, p_2, \ldots, p_6$ are calculated by 2nd order finite differences.

3. Method by Euler Equations

It is very effective to investigate the flowfield around ATP by solving 3D-Euler equations. L.J.Bober et al. succeeded to do this and got the results until flight Mach number 0.8. The procedures employed in this paper follow those by Refs. 5 and 6. The descriptions will be abbreviated and the detail should be refered to the references.

3.1 Basic Equations

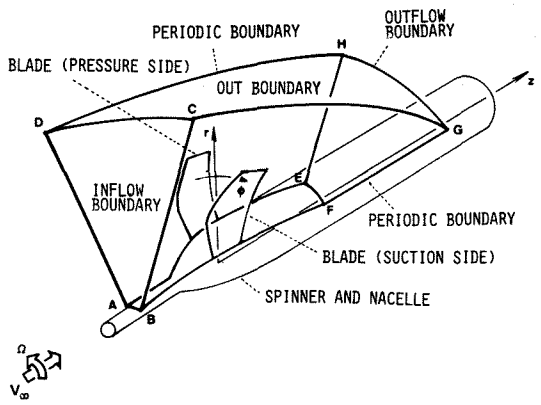

Fig.4 Physical space and coordinate axes

Although the rotating frame fixed to the blade was chosen in the potential analysis, the static coordinate system is utilized in this Euler case. Fig.4 shows the physical space with the cylindrical coordinates in which z is adverse direction of ATP motion, r extends radially outward from z-axis and ϕ is the meridional angle measured from the vertical plane. The Euler equations in weak conservation law form are given by

$$Q_t + E_z + F_r + \frac{1}{r}G_\phi + H = 0, \tag{28}$$

where

$$Q = \begin{bmatrix} \rho \\ \rho u \\ \rho v \\ \rho w \\ e \end{bmatrix} \quad E = \begin{bmatrix} \rho u \\ \rho u^2+p \\ \rho uv \\ \rho uw \\ (e+p)u \end{bmatrix} \quad F = \begin{bmatrix} \rho v \\ \rho uv \\ \rho v^2+p \\ \rho vw \\ (e+p)v \end{bmatrix}$$

$$G = \begin{bmatrix} \rho w \\ \rho uw \\ \rho vw \\ \rho w^2+p \\ (e+p)w \end{bmatrix} \quad H = \begin{bmatrix} \rho v \\ \rho uv \\ \rho(v^2-w^2) \\ 2\rho vw \\ (e+p)v \end{bmatrix} \tag{29}$$

$$e = \frac{p}{\gamma - 1} + \frac{1}{2}(u^2 + v^2 + w^2) \tag{30}$$

In the above equations u, v and w are the cylindrical velocity components along z, r and ϕ-directions respectively, and e is the total energy per unit volume.

By this relation, the pressure is calculated. Furthermore, the pressure p, density ρ and velocity components u, v and w are nondimensionalized by p_∞, ρ_∞ and $a_\infty\sqrt{\gamma}$ respectively, where ∞ indicates the value at the free-stream.

The cylindrical coordinates are transformed into the computational domain by

$$\begin{aligned}\tau &= t\\ \xi &= \xi(t,z,r,\phi)\\ \eta &= \eta(t,z,r,\phi)\\ \zeta &= \zeta(t,z,r,\phi)\end{aligned} \tag{31}$$

This generalized nonorthogonal coordinate transformation maps the nacelle surface into a constant η-plane and both sides of the blade into two constant ζ-planes. Then, the Euler equations, Eq.(28), are rewritten by the transformation as follows:

$$\hat{Q}_\tau + \hat{E}_\xi + \hat{F}_\eta + \hat{G}_\zeta + \hat{H} = 0, \tag{32}$$

where

$$\hat{Q} = J\begin{bmatrix}\rho\\ \rho u\\ \rho v\\ \rho w\\ e\end{bmatrix} \quad \hat{E} = J\begin{bmatrix}\rho U\\ \rho uU+p\xi_z\\ \rho vU+p\xi_r\\ \rho wU+p\xi_\phi/r\\ (e+p)U-p\xi_t\end{bmatrix} \quad \hat{F} = J\begin{bmatrix}\rho V\\ \rho uV+p\eta_z\\ \rho vV+p\eta_r\\ \rho wV+p\eta_\phi/r\\ (e+p)V-p\eta_t\end{bmatrix}$$

$$\hat{G} = J\begin{bmatrix}\rho W\\ \rho uW+p\zeta_z\\ \rho vW+p\zeta_r\\ \rho wW+p\zeta_\phi/r\\ (e+p)W-p\zeta_t\end{bmatrix} \quad \hat{H} = \frac{J}{r}\begin{bmatrix}\rho v\\ \rho uv\\ \rho(v^2-w^2)\\ 2\rho vw\\ (e+p)v\end{bmatrix} \tag{33}$$

$$J = \frac{(z,r,\phi)}{(\xi,\eta,\zeta)} = z_\xi r_\eta \phi_\zeta + r_\xi \phi_\eta z_\zeta + \phi_\xi z_\eta r_\zeta - z_\xi r_\zeta \phi_\eta - r_\xi \phi_\zeta z_\eta - \phi_\xi z_\eta r_\zeta, \tag{34}$$

and

$$\begin{aligned}U &= \xi_t + u\xi_z + v\xi_r + w\xi_\phi/r\\ V &= \eta_t + u\eta_z + v\eta_r + w\eta_\phi/r\\ W &= \zeta_t + u\zeta_z + v\zeta_r + w\zeta_\phi/r\end{aligned} \tag{35}$$

These U, V and W are the contravariant velocity components. The derivatives ξ_τ, ξ_z etc. are obtained by chain rule.

3.2 Mesh Generations and Computational Domain

The mesh generation procedures are basically same with the potential case described in 2.2. In this Euler case, however, the flowfield between neighboring blades is calculated. Therefore, the new physical space is made by rotating the periodic plane by π/B rad.(B : number of blades). The new periodic planes are the outside parts of the suction and pressure sides of the blade. Moreover, the mesh lines on the outer boundary were spirally tilted in the potential case, however, these are approximately straight

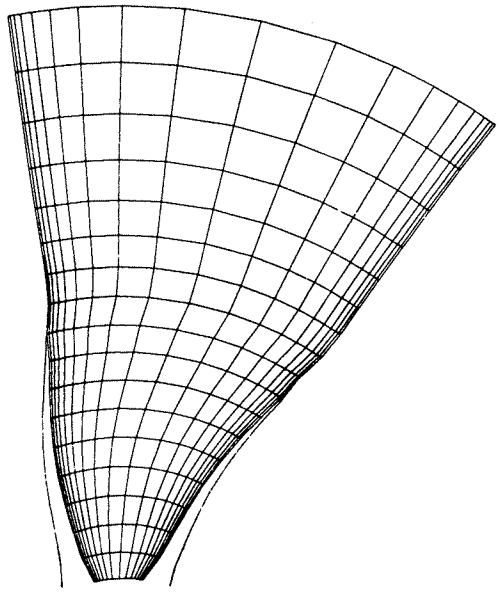

(a) ξ-constant plane

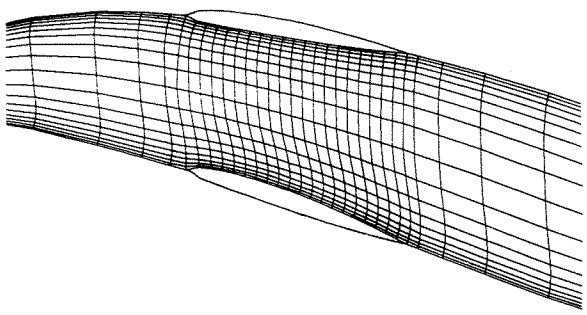

(b) η-constant plane

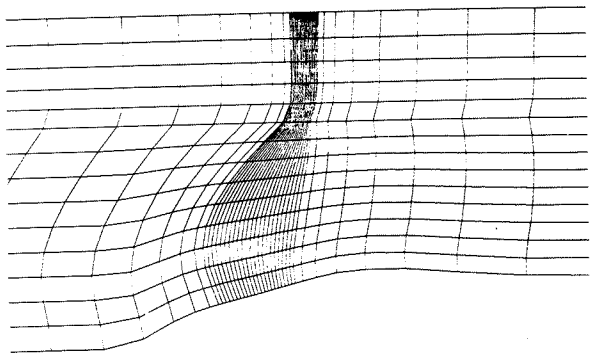

(c) ζ-constant plane

Fig.5 Meshes around the SR-3 propeller

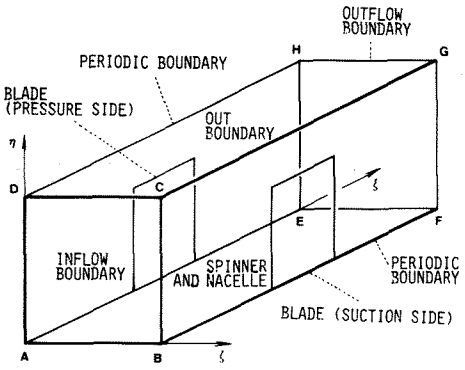

Fig.6 Computational domain

in this case, because the system of coordinate axes are static. Instead of the rotating axes, all over the mesh system rotates in this case with rotating speed of the propeller. The pitch angle of the outer hypothetical blades changes gradually until zero at the outer boundary. The meshes generated are shown in Figs.5(a), (b) and (c) which correspond to ξ-, η- and ζ-constant planes in the computational domain respectively, which is shown in Fig.6.

3.3 Method of Numerical Calculations

The numerical algorithm used to solve the Euler equations, Eq.(32), which have the conservation law form is non-iterative, implicit ADI schemes. The scheme employed in this calculation is the scheme developed by Beam and Warming[11] Letting the duration of mesh of computational domain be unity, i.e. $\Delta\xi = \Delta\eta = \Delta\zeta = 1$, the AF scheme takes the following form.

$$
\begin{aligned}
&[I + \Delta t\delta_\xi \hat{A}^n - e_i(J\nabla_\xi\Delta_\xi J^{-1})^n] \\
&\times[I + \Delta t\delta_\eta \hat{B}^n - e_i(J\nabla_\eta\Delta_\eta J^{-1})^n] \\
&\times[I + \Delta t\delta_\zeta \hat{C}^n - e_i(J\nabla_\zeta\Delta_\zeta J^{-1})^n]\ (Q^{n+1} - Q^n) \\
&= -\Delta t[\delta_\xi \hat{E}^n + \delta_\eta \hat{F}^n + \delta_\zeta \hat{G}^n + \hat{H}^n] \\
&\quad - e_e J^n[(\nabla_\xi\Delta_\xi)^2 + (\nabla_\eta\Delta_\eta)^2 + (\nabla_\zeta\Delta_\zeta)^2]\ (J^{-1}\hat{Q})^n,
\end{aligned}
\tag{36}
$$

where $\hat{A}$, $\hat{B}$ and $\hat{C}$ are Jacobian matrices, i.e. $\partial\hat{E}/\partial\hat{Q}$, $\partial\hat{F}/\partial\hat{Q}$ and $\partial\hat{G}/\partial\hat{Q}$ respectively. These are expressed by Jacobian matrices $A(=\partial E/\partial Q)$, $B(=\partial F/\partial Q)$ and $C(=\partial G/\partial Q)$ as follows:

$$
\hat{A} = \partial\hat{E}/\partial\hat{Q} = k_0 I + k_1 A + k_2 B + \frac{k_3}{r}C, \tag{37}
$$

where

$$
k_0 = \xi_t,\ k_1 = \xi_z,\ k_2 = \xi_r,\ k_3 = \xi_\phi, \tag{38}
$$

and I is the identity matrix. The detailed expressions are given in Refs.5 or 6. The terms multiplied by e_i in the left hand side and by e_e in the right hand side are added for dissipation. The former controls the instability, and the latter is added to decrease the short wavelength oscillations.

In transonic flowfield, the difference scheme should be switched whether the flow velocity is subsonic or supersonic in order to get the stable solution. In this case, only δ_ξ is calculated using the following procedure.

$$
\delta_\xi f|_i = \frac{\mu\delta_\xi(\nabla_\xi\varepsilon_i\Delta_\xi/2)}{\Delta\xi}\,\frac{1}{1 - (\nabla_\xi\varepsilon_i/2)}\,f_i^n \tag{39}
$$

where ε_i is switching operater given as follows:

$$
\varepsilon_i = \begin{cases} 0 & : \text{subsonic} \\ 1 & : \text{supersonic} \end{cases} \tag{40}
$$

By Eq.(39), differencing transfers from central difference to upwind one smoothly as the flow velocity changes from subsonic to supersonic. The other differentiations δ_η and δ_ζ are approximated by the central difference. The second term of the numerater of Eq.(39) is calculated as follows:

$$
\begin{aligned}
\nabla_\xi\varepsilon_i\Delta_\xi f_i &= \nabla_\xi\varepsilon_i(f_{i+1}^n - f_i^n) \\
&= \varepsilon_{i-1}f_{i-1}^n - (\varepsilon_{i-1} + \varepsilon_i)f_i^n + \varepsilon_i f_{i+1}^n
\end{aligned}
\tag{41}
$$

In order to solve Eq.(36), that is, to solve Q^{n+1}, the following four step sequential processes are executed.

$$
\begin{aligned}
&[I + \Delta t\delta_\xi \hat{A}^n - e_i(J\nabla_\xi\Delta_\xi J^{-1})^n]\Delta\hat{Q}^* = RHS^n \\
&[I + \Delta t\delta_\eta \hat{B}^n - e_i(J\nabla_\eta\Delta_\eta J^{-1})^n]\Delta\hat{Q}^{**} = \Delta\hat{Q}^* \\
&[I + \Delta t\delta_\zeta \hat{C}^n - e_i(J\nabla_\zeta\Delta_\zeta J^{-1})^n]\Delta\hat{Q}^n = \Delta\hat{Q}^{**} \\
&\hat{Q}^{n+1} = \hat{Q}^n + \Delta\hat{Q}^n,
\end{aligned}
\tag{42}
$$

where ΔQ^* and ΔQ^{**} are intermediate values of the first and second inversions respectively. RHS^n expresses the right hand side of Eq.(36). This term is calculated at each mesh point before the inversion steps. ΔQ^{n+1} tends to a constant steady value as time t increases. The calculation stops as the convergence is reached when the average value of ΔQ^n comes to or less than 10^{-4}. According to the linear stability analysis, the implicit AF method is unconditionally stable. However, the increment of time, Δt, has a limited value.

3.4 Boundary Conditions

(1) Inflow and out-boundary conditions

The variation of all quantities should be zero at the inflow and out-boundary, i.e.

$$
\Delta\hat{Q}_{ABCD} = \Delta\hat{Q}_{CGHD} = 0 \tag{43}
$$

(2) Outflow conditions

When the flowfield is subsonic, only the pressure has to show no change, i.e.

$$
\Delta p = 0 \tag{44}
$$

The other quantities are extrapolated at the outflow boundary.

(3) Tangency conditions on the solid surfaces

On the blade and nacelle surfaces, the contravariant velocities should be zero because of their tangency.

$$
\begin{aligned}
&W = 0 \quad : \quad \text{blade} \\
&V = 0 \quad : \quad \text{nacelle}
\end{aligned}
\tag{45}
$$

Moreover, both contravariant velocities should be zero simultaneously on the intersection of the blade and nacelle. The velocity components on the solid surfaces are obtained by the linear extrapolation. For example, U and V are obtained by linear extrapolation while W = 0 by the tangency condition on the blade. Therefore, u, v and w are calculated by the following equations.

$$\begin{bmatrix} u \\ v \\ w \end{bmatrix} = J \begin{bmatrix} (\eta_r\zeta_\phi - \eta_\phi\zeta_r)/r & -(\xi_r\zeta_\phi - \xi_\phi\zeta_r)/r \\ -(\eta_z\zeta_\phi - \eta_\phi\zeta_z)/r & (\xi_z\zeta_\phi - \xi_\phi\zeta_r)/r \\ (\eta_z\zeta_r - \eta_r\zeta_z) & -(\xi_z\zeta_r - \xi_r\zeta_z) \end{bmatrix}$$

$$\begin{bmatrix} (\xi_r\eta_\phi - \xi_\phi\eta_r)/r \\ -(\xi_z\eta_\phi - \xi_\phi\eta_r)/r \\ (\xi_z\eta_r - \xi_r\eta_z) \end{bmatrix} \begin{bmatrix} U - \xi_t \\ V - \eta_t \\ W - \zeta_t \end{bmatrix} \quad (46)$$

(4) Periodic boundaries

As Fig.9 shows, the periodic boundaries locate at the outside parts of the suction and pressure sides of the blade in this Euler case. The values of two points which correspond with each other should be equal on the periodic boundaries.

$$\hat{\Delta Q}_{AEHD} = \hat{\Delta Q}_{BFGC} \quad (47)$$

As the initial condition at t = 0, the free-stream velocity field is given, and the time marching process starts.

4. Numerical Results

The numerical calculations were performed for SR-3 where the pitch angle at three quarter of the tip radius, $\beta_{0.75R}$ are 57.3, 59.3 and 61.3 deg., and the range of advance ratio is from 3 to 4. The flight Mach number M_∞ is 0.8. The number of meshes are 51 along x direction, 16 along y direction and 21 along z direction for the potential case, and 45 along z direction, 18 along r direction and 19 along ϕ direction for the Euler case (see Fig.2 and Fig.5). The initial values were set to zero and the relaxation factor was 0.9 throughout the potential calculations. The free-stream velocity field was given as initial values for the Euler cases. Dissipation coefficients e_i and e_e in Eq.(36) took the various values according to the pitch angles and advance ratios.

Pressure distributions on the suction and pressure surfaces of the blade and isolines of constant relative Mach numbers are shown in Figs.7(potential case) and 8(Euler case). The pitch angle at three-quarter of the tip radius is 59.3 deg. The isobars and relative Mach numbers above and below the blade are shown in Figs.9(potential case) and 10(Euler case). Figs.7 and 8 show that shock waves appear on the suction sides near trailing edge. Comparing these figures with each other and with the results obtained by Bober et al., pressure and iso-Mach lines are different delicately. However, the overall tendencies agree with each other. The same can be described for the figures of the flowfield above and below the blade. The degree of convergence is good until the flight Mach number is 0.8.

Finally, the aerodynamic performances of SR-3 at M_∞ = 0.8 are shown in Fig.11. Since the potential cannot give drag force, the results of the potential cases are obtained by using the experimental drag force of NACA 16 series airfoil sections as the similar manner of Ref.3. Comparing these calculations with the experimental results, both of power coefficients and efficiencies are larger than those of experiments. The reason of these facts are estimated as follows: First, recovering moments by centrifugal force act on the blade. Therefore, the actual pitch angle is smaller than the nominal one. This phenomenon was indicated in the discussions of Ref.3. The angle at three-quarter of the tip radius was 1.3 deg. smaller than the set angle by the calculations through NASTRAN. Second, the shock wave on the actual ATP blade might be stronger than that in the calculation. Therefore, isentropic assumption might be violated in the experiments. However, the Euler cases are closer than the potential cases by the reason that the effects of tip vortex and viscosity cannot be estimated by the potential analysis.

The computer systems used for these calculations were FACOM M-382 and VP-200 vector processor at Kyoto University Data Processing Center. CPU-time for one case calculation was about 15 minutes for the potential case, and 30 minutes for the Euler case, while that for the VLM was about 2 minutes.

5. Conclusion

It is very important to investigate the flowfield around ATP for its optimal design. In order to accomplish this, the numerical methods are appropriate. The wind-tunnel tests might accompany difficulties. Among several numerical techniques, the finite difference methods are better for this purpose because of transonic flowfield around ATP. We can solve both of potential equation and Euler equations by this method. Although the flowfield detail can be clarified with accuracy by solving 3D-Euler equations, CPU-time takes longer. On the contrary, it is relatively short for the potential equation. In this investigation, the flowfield around an ATP are calculated by both methods.

If the frame is fixed on a blade, flow becomes steady, but rotating. Since no full potential exist in this flowfield, the equation for a disturbance velocity potential is solved without any linearization. Boundary fitted meshes are generated around ATP. The transformations between physical space and computational one can be performed by chain rule. These computational meshes expanding the space between two periodic boundaries including a blade. The line relaxation method is used for solving equation. All derivatives are calculated by second order central differences. The artificial viscosity is introduced as the directional bias in supersonic domain.

On the contrary, the static cylindrical coordinate system is employed in order to solve the Euler equations. Although the same method with the potential case for generation of meshes around the ATP is utilized, the physical space chosen for this case is that between the neighboring blades. The non-iterative, implicit ADI schemes are used for the numerical algorithm, and AF scheme is employed to obtain the steady state solutions.

SR-3 is used for numerical calculations and the results of two methods show qualitative agreement

with each other and with the results by Bober et al. Finally, we obtained the aerodynamic performances such as power coefficients and efficiencies, and these values are relatively larger than the experimental values obtained at NASA. The reasons of this difference are due to (1) recovering of pitch angle by centrifugal force, (2) violation of isentropic assumption. It should be noted that the results by the Euler analysis are closer to the experimental values than the potential case.

Acknowledgements

The authors would like to acknowledge helpful discussions with Dr. H.Takeda of the Department of Aeronautical Engineering of Kyoto University.

References

1. Sullivan, J. P., "The Effect of Blade Sweep on Propeller Performance", AIAA Paper 77-716,1977.
2. Hanson, D. B., "Compressible Helicoidal Surface Theory for Propeller Aerodynamics and Noise", AIAA Journal, Vol.21, June, 1983, pp.881-889.
3. Kobayakawa, M. and Onuma, H., "Propeller Aerodynamic Performance by Vortex-Lattice Mehtod", Journal of Aircraft, Vol.22, August, 1985, pp.649-654.
4. Jou, W. H., "Finite Volume Calculation of Three-Dimensional Potential Flow Around a Propeller", AIAA Journal, Vol.21, Oct, 1983, pp.1360-1364.
5. Chaussee, D. S. and Kutler, P., "User's Manual for Three-Dimensional Analysis of Propeller Flow Fields", NASA CR-167959, Jan., 1983.
6. Bober, L. J. et al., "Prediction of High Speed Propeller Flow Fields Using a Three-Dimensional Euler Analysis", AIAA Paper 83-0188, 1983.
7. Bousquet, J. M., "Methodes Aerodynamiques Utilisees en France pour L'etude des Helices pour Avions Rapides", La Recherche Aerospaciale, Jan.-Feb., 1985, pp.1-15.
8. Rohrbach, C. et al., "Evaluation of Wind Tunnel Performance Testings of an Advanced 45° Swept Eight-Bladed Propeller at Mach Number from 0.45 to 0.85", NASA CR 3505, 1982.
9. Dulikravich, D. S., "Fast Generation of Three-Dimensional Computational Boundary-Conforming Periodic Grids of C-Type", Numerical Grid Generation, Elsevier Science Publishing, 1982, pp.563-584.
10. Chen, L. T., "A More Accurate Transonic Computational Method for Wing-Body Configurations", AIAA Journal, Vol.21, June, 1983, pp.848-855.
11. Beam, R. M. and Warming, R. F., "An Implicit Finite-Difference Algorithm for Hyperbolic Systems in Conservation-Law Form", Journal of Computational Physics, Vol.22, 1976, pp.87-110.

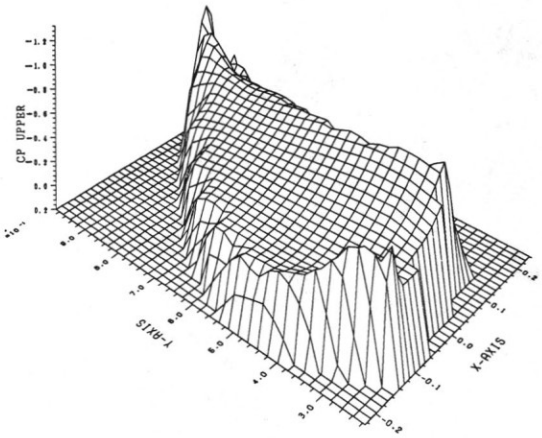

Suction side

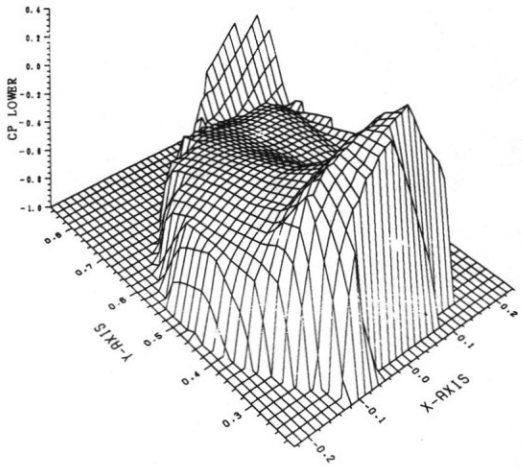

Pressure side
Pressure distributions

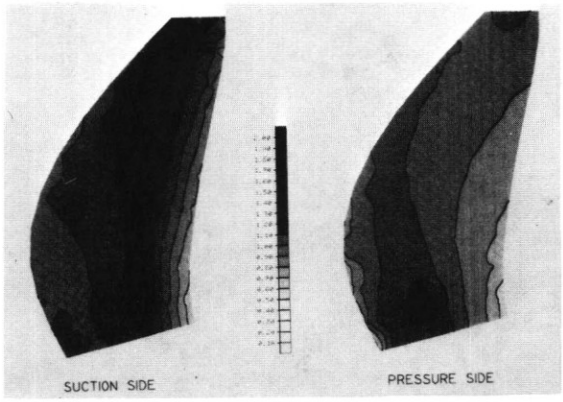

Iso-Mach lines

Fig.7 Pressure distributions and iso-Mach lines of the SR-3 propeller by potential analysis ($\beta_{0.75R}$ = 59.3°, J = 3.5)

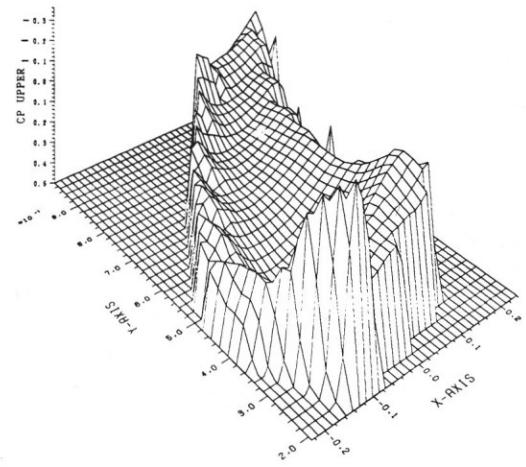

Suction side

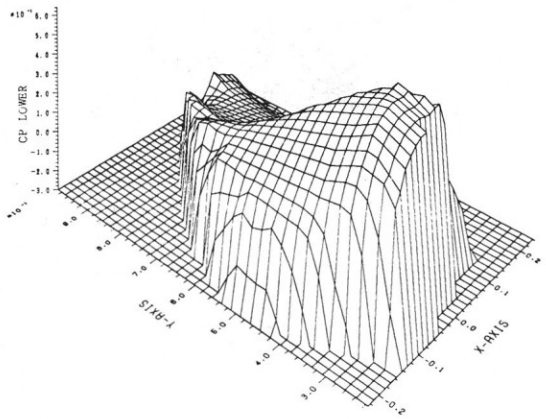

Pressure side
Pressure distributions

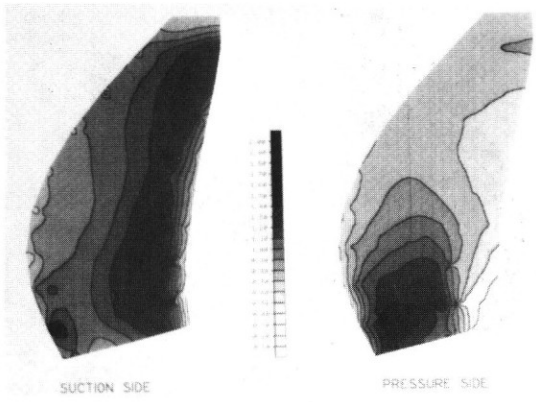

Iso-Mach lines
Fig. 8 Pressure distributions and iso-Mach lines of the SR-3 propeller by Euler analysis
($\beta_{0.75R}$ = 59.3°, J = 3.4)

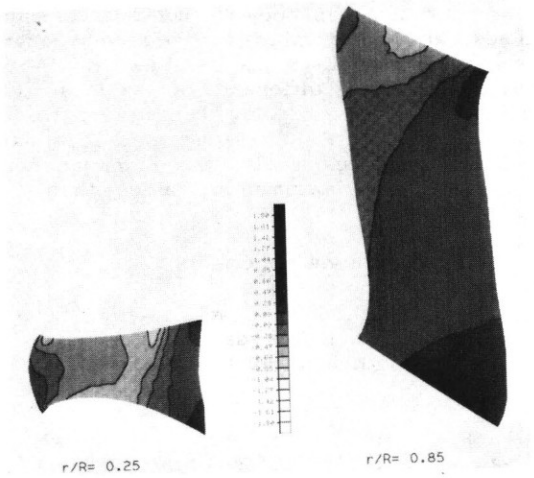

Iso-bars

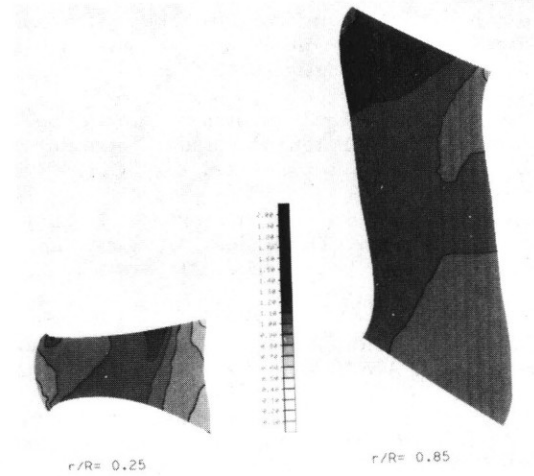

Iso-Mach lines
Fig. 9 Iso-bars and iso-Mach lines of the SR-3 propeller by potential analysis
($\beta_{0.75R}$ = 59.3°, J = 3.5)

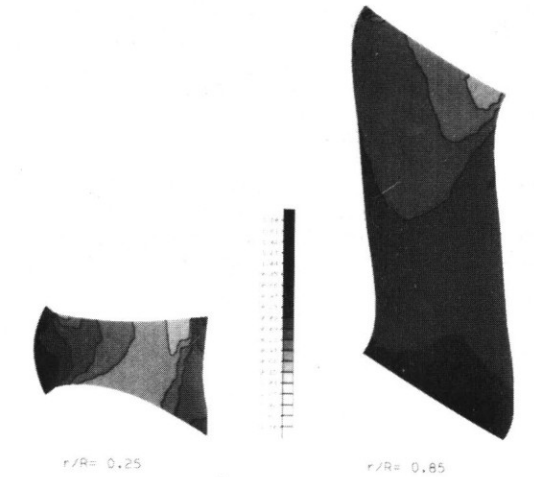

Iso-bars

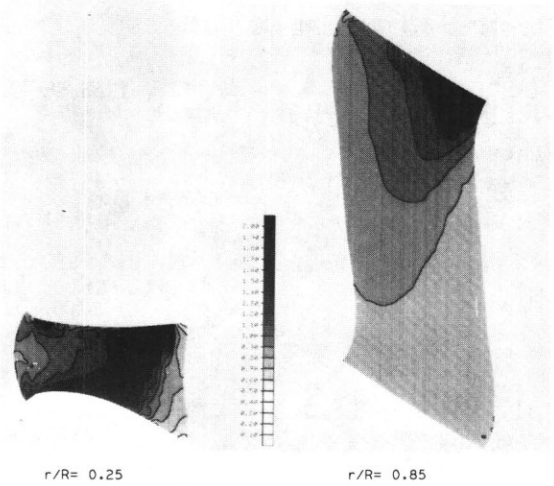

Iso-Mach lines
Fig. 10 Iso-bars and iso-Mach lines
of the SR-3 propeller by Euler analysis
($\beta_{0.75R}$ = 59.3°, J = 3.4)

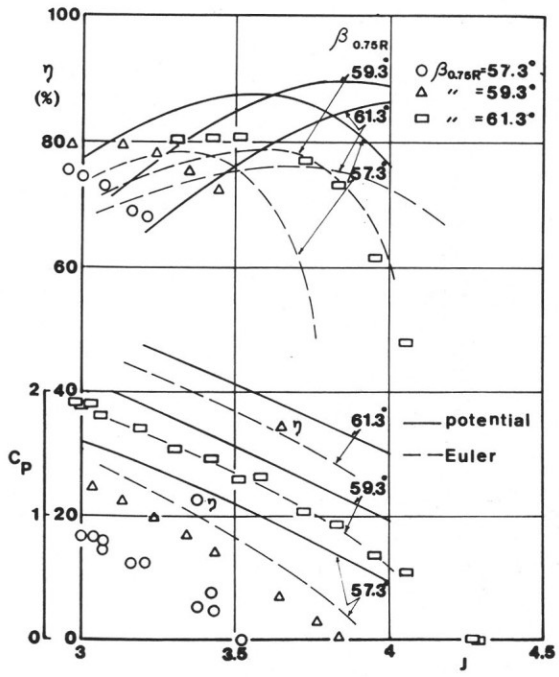

Fig. 11 Power coefficients and efficiencies
of the SR-3 propeller